Analytical and Bioanalytical Chemistry (2022) 414:1909–1919
https://doi.org/10.1007/s00216-021-03826-2

RESEARCH PAPER

Directed self-assembly of Ag^+-deposited MoS_2 quantum dots for colorimetric, fluorescent and fluorescence-lifetime sensing of alkaline phosphatase

Manivannan Madhu[1] · Chien-Min Chao[2] · Chen-Yi Ke[1] · Ming-Mu Hsieh[2] · Wei-Lung Tseng[1,3]

Received: 29 September 2021 / Revised: 6 November 2021 / Accepted: 2 December 2021 / Published online: 23 January 2022

Abstract

We developed a triple-readout probe for colorimetric, fluorescent, and fluorescence-lifetime sensing of alkaline phosphatase (ALP) through the hydrolyzed ascorbic acid phosphate (AAP)–mediated formation of silver nanoparticles (AgNPs) on Ag^+-deposited MoS_2 quantum dots (QDs). Ag^+ ions were self-assembled on a monolayer MoS_2 QD surface through the formation of Ag–S bonds. When ALP hydrolyzed AAP in an alkaline buffer, the resultant ascorbic acid (AA) triggered the reduction of the bound Ag^+ ions into AgNPs on the MoS_2 QD surface. The resultant AgNPs induced an efficient fluorescence quenching of the MoS_2 QDs through simultaneous static and dynamic quenching processes, generated an intense surface plasmon resonance peak, and triggered a reduction in the fluorescence lifetime of the MoS_2 QDs. Electron microscopy and spectroscopic techniques revealed the successful fabrication of Ag^+-deposited MoS_2 QDs and the ALP-mediated formation of AgNPs on the MoS_2 QD surface. The linear quantification ranges for ALP were 0.05–2.5, 0.1–4, and 1–4 units L^{-1} in the fluorescent, colorimetric, and fluorescence-lifetime detection modes, respectively. In addition, the proposed probe integrated with an ALP-linked sandwich immunoassay exhibited high sensitivity and selectivity for the fluorescence sensing of rabbit immunoglobulin G with a detection limit of 8 pg mL^{-1} and linear range of 25–1000 pg mL^{-1}. The sensitivity of the probe is comparable to those of previously reported immunoassays involving ultrasensitive electrochemical detection, hydrogen evolution reactions, or electron spin resonance. The probe integrated with the sandwich assay serves as a promising platform for the detection of target proteins in clinical samples.

Keywords Alkaline phosphatase · Triple-modal sensors · MoS_2 quantum dots · Silver nanoparticles · Immunoassay

Introduction

Alkaline phosphatase (ALP), a zinc-containing dimeric enzyme, is profoundly connected with phosphate metabolism in biological systems. ALP catalyzes the cleavage of phosphomonoester bonds in biomolecules, such as adenosine 5′-triphosphate (ATP) and pyrophosphate [1]. The catalytic activity of ALP depends on environmental conditions (e.g., pH and temperature) and substrates [2] and enables the evaluation of the number of specific substrates involved in biological events in humans. Because the average level of serum ALP in adults (46–190 units L^{-1}) is much lower than that in children (> 500 units L^{-1}) due to bone growth [3], ALP has long been recognized as a prominent biomarker in the diagnosis of bone diseases [4]. Elevated serum ALP levels are associated with various diseases, including prostate cancer [5], breast cancer [6], diabetes [7], and liver dysfunction [8]. In addition, ALP-linked antibodies are often utilized

Manivannan Madhu and Chien-Min Chao contributed equally to this work.

✉ Ming-Mu Hsieh
t3644@nknucc.nknu.edu.tw

✉ Wei-Lung Tseng
tsengwl@mail.nsysu.edu.tw

[1] Department of Chemistry, National Sun Yat-Sen University, Taiwan, Republic of China

[2] Department of Chemistry, National Kaohsiung Normal University, Taiwan, Republic of China

[3] School of Pharmacy, College of Pharmacy, Kaohsiung Medical University, Taiwan, Republic of China

as signal reporters in enzyme-linked immunosorbent assays (ELISAs), which are versatile platforms for the sensitive and selective detection of bioactive molecules [9, 10] and organic pollutants [11, 12] in aqueous samples. By taking advantage of the specific recognition between an antibody and antigen, antibody–ALP conjugates trigger the hydrolysis of phosphate-containing substrates to produce an amplified signal, which allows for the detection of low concentrations of the target antigen [13] with high specificity. In addition to playing a key role in physiological events, ALP and its derivatives often serve as sensing components or reporters in bioanalytical studies. Accordingly, the development of a reliable, sensitive, and robust method for the identification and quantification of ALP in biological samples is a priority.

Traditional methods for detecting ALP activity include the ALP-mediated dephosphorylation of radioactive pyrophosphate [14] and the measurement of released phosphate from the ALP-triggered cleavage of pyrophosphate [15]. However, these methods may cause problems related to the production of radioactive waste during radionuclide quantification. Recently, a series of sensing strategies have been introduced for the determination of ALP activity based on the monitoring of ALP-induced hydrolysis of phosphate-bearing compounds using electrochemical and spectroscopic techniques [16–18]. Examples of phosphate-containing substrates include pyrophosphate [19], ATP [20], 4-methylumbelliferyl phosphate [21], *p*-nitrophenyl phosphate [22], and L-ascorbic acid 2-phosphate (AAP) [23]. In contrast to most ALP substrates, AAP can release L-ascorbic acid (AA) with reducing ability after the cleavage of phosphomonoester bonds in the presence of ALP. Thus, numerous fluorometric and colorimetric probes have been introduced for ALP sensing through AA-mediated reduction. In principle, the resultant AA molecules (1) trigger the fluorescence reaction with small organic molecules [24–26], (2) induce the fluorescence of metal ion-chelating molecules [27] and nanomaterials [28], (3) inhibit H_2O_2-related catalytic reactions with colorimetric probes [29], (4) promote the reduction of MnO_2 nanosheets [30], and (5) induce the reduction of metal ions to form plasmonic metal nanoparticles [31] and fluorescent metal nanoclusters [32] in the absence or presence of a nanostructure surface. Although they exhibit high sensitivity and selectivity toward ALP, most of the aforementioned methods generate a single-mode signal output during the sensing process. An increasing number of studies are employing multidimensional signal probes because they provide reliable results for the accurate and precise quantification of heavy metal ions [33, 34], small molecules [35, 36], and ALP [37]. For example, Zhao et al. developed a colorimetric and fluorometric platform to detect ALP activity through three successive reactions, namely ALP-induced hydrolysis of *p*-aminoethyl-phenyl phosphate to tyramine, tyrosinase-mediated conversion of tyramine to dopamine, and reaction of dopamine and resorcinol [38]. The same research group also utilized *m*-hydroxyphenyl phosphate as an ALP substrate for the colorimetric and fluorometric detection of ALP activity in the presence of dopamine [39]. Chen et al. performed a colorimetric and fluorometric dual-readout assay of ALP based on three concepts: (1) the ALP-mediated hydrolysis of AAP to AA, (2) the AA-induced reduction of Ag^+ ions on the surface of gold nanoparticles, and (3) the inner filter effect of silver-coated gold nanoparticles on the fluorescence of graphene quantum dots (QDs) [40]. Zhang et al. determined that AA resulting from ALP-catalyzed hydrolysis of AAP triggers the aggregation of 4-mercaptophenylboronic acid (4-MPBA)–modified silver-coated gold nanoparticles, leading to the color change of the nanoparticles and the amplification of Raman scattering of the 4-MPBA [41]. However, few studies have employed multimodal assays of ALP, which are expected to provide more accurate results than do the aforementioned methods.

The last several years have witnessed the broad application of molybdenum disulfide (MoS_2) QDs in electrocatalysts [42], lithium storage [43], bioimaging [44], gas sensing [45], and biosensors [46]. Compared with organic fluorophores and nanomaterials, MoS_2 QDs possess unique properties that include excitation-dependent emission, high photobleaching resistance, strong two-photon absorption, and surface sulfur vacancy sites. Additionally, MoS_2 nanosheets with exposed sulfur atoms can be utilized to remove Ag^+ ions from an aqueous solution [47]. On the basis of this concept, in this study, we successfully prepared Ag^+-deposited MoS_2 QDs and applied them in a trimodal (colorimetric, fluorescence, and fluorescence-lifetime modes) sensor to detect ALP. After ALP catalyzed the hydrolysis of AAP, the resultant AA triggered the reduction of the bound Ag^+ ions on the MoS_2 QD surface. The resultant silver nanoparticles (AgNPs) had a new surface plasmon resonance (SPR) band in the visible region and quenched the fluorescence of and induced a reduction in the fluorescence lifetime of the MoS_2 QDs. The integration of the Ag^+-modified MoS_2 QDs into an ALP-related sandwich immunoassay was further utilized for the dual-detection of spiked rabbit immunoglobulin (IgG) in human plasma samples. The integration of the Ag^+-deposited MoS_2 QDs into an ALP–AAP reaction was further utilized for the colorimetric, fluorescent, and fluorescence-lifetime sensing of ALP in human plasma samples.

Materials and methods

Chemicals Silver nitrate, AA, AAP, 4-(2-hydroxyethyl)-1-piperazineethane sulfonic acid (HEPES), N,N-dimethylformamide (DMF), anti-rabbit IgG antibody, and ALP (from bovine intestinal mucosa), thrombin (from bovine plasma), lysozyme (from egg white), glucose oxidase (from

Aspergillus niger), horseradish peroxidase (from horseradish roots), human serum albumin (from human plasma), and bovine serum albumin (from bovine plasma) were purchased from Sigma-Aldrich (St. Louis, MO, USA). MoS_2 ultrafine powder was ordered from Alfa Aesar (Ward Hill, MA, USA). ALP-labeled anti-rabbit IgG was purchased from AnaSpec, Inc. (San Jose, CA, USA). All other chemical reagents were of analytical grade. Ultrapure water (Millipore, Germany) was used throughout the whole experiment.

Synthesis and characterization of MoS_2-related nanomaterials The synthesis of the MoS_2 QDs was conducted according to our recently published procedure [46–49]. Layered MoS_2 materials (0.04 g) were added to DMF (40 mL) in a scintillation bottle (50 mL); then, ultrasonication (Elmasonic E60H, Elma, Singen, Germany) was performed at 150 W for 30 h under an ice bath. To remove the multilayered MoS_2 materials, the as-prepared solution was centrifuged at 6000 rpm (25 °C ambient) for 30 min. The obtained supernatant was transferred into a round-bottle flask (50 mL) and heated in an oil bath (145 °C) for 8 h under vigorous stirring. The dried MoS_2 QDs were redispersed in ultrapure water (40 mL) and stored at 4 °C for further use. The MoS_2 QDs could then be stabilized in an aqueous solution for several months for long-term storage. The morphology of the MoS_2-related nanomaterials was imaged using transmission electron microscopy (TEM; JEM-2100, JEOL, Japan; 200 kV) integrated with energy-dispersive X-ray spectroscopy (EDS). The zeta potential of the nanomaterials was measured using a DelsaNano zeta potential analyzer (Beckman Coulter, Brea, CA, USA). A small aliquot of the MoS_2 QDs solution was removed and dried in an 80 °C oven to determine the weight per volume of the MoS_2 QDs. The mass concentration of the MoS_2 QDs was 1 mg mL^{-1}. The estimated number of MoS_2 QDs per unit volume was 5.6×10^{17} particles mL^{-1} and was calculated by dividing the mass concentration by the mass of a single MoS_2 QD. According to the data from the TEM and atomic force microscopy, the volume ($3.14\times r^2\times h$) of a single MoS_2 QD used in this study was 2.8 nm^3. Thus, using the density (5.06 g cm^{-3}) of bulk MoS_2, the mass of a single MoS_2 QD was determined to be 1.8×10^{-21} g.

Triple-channel sensing of ALP activity To detect ALP activity, the MoS_2 QDs (1 mg mL^{-1}, 100 µL) were initially equilibrated with Ag^+ (100 mM, 100 µL) in 20 mM Tris–borate buffer (pH 9.8) at ambient temperature for 10 min. When the added Ag^+ ions were entirely adsorbed on the MoS_2 QD surface, approximately 110 Ag^+ ions were present on each MoS_2 QD. Samples with various concentrations of ALP (0–10 units L^{-1}, 500 µL) reacted with a fixed concentration of AAP (32 mM, 300 µL) at 37 °C for 30 min. The Ag^+-deposited MoS_2 QDs (200 µL; 0.5 mg mL^{-1} of MoS_2 QDs and 50 mM Ag^+) were introduced into the resultant solution. The mixture was vigorously vortexed at ambient temperature for 10 min. The fluorescence spectra, absorption spectra, and fluorescence lifetime decay of the resultant solution were recorded on a fluorometer (Hitachi F-7000, Hitachi, Tokyo, Japan) at an excitation wavelength of 340 nm, an ultraviolet–visible spectrophotometer (JASCO V-670, JASCO, Tokyo, Japan), and a time-correlated single-photon counting device (Time-Harp 200, PicoQuant, Berlin, Germany) integrated with a 390-nm pulsed diode laser (with a pulse width of tens of ps), respectively. To verify the selectivity of the proposed system and the substrate specificity of ALP, we substituted ALP with other proteins, including thrombin (from bovine plasma), lysozyme (from egg white), glucose oxidase (from *Aspergillus niger*), horseradish peroxidase (from horseradish roots), human serum albumin (from human plasma), and bovine serum albumin (from bovine plasma).

Fluorescence immunoassay The sandwich immunoassay for detecting IgG was conducted by following the standard protocol with slight modification [50]. Briefly, the coating solution (100 µL) consisting of anti-rabbit IgG (5 µg mL^{-1}) and 25 mM sodium carbonate (pH 9.6) was pipetted into each well (96-well polystyrene plate) and then let stand at 4 °C for 12 h. Afterward, the coating solution was discarded to remove excess anti-rabbit IgG. Each well was incubated with the blocking solution (200 µL; pH 7.5, 3% w/v BSA, 100 mM Tris–HCl, 150 mM NaCl, and 0.05% v/v Tween 20) at ambient temperature for 1 h. The resulting wells were rinsed three times with the washing solution (200 µL; pH 7.5, 100 mM Tris–HCl, 150 mM NaCl and 0.05% v/v Tween 20), incubated with rabbit IgG (0.01–5 ng mL^{-1}, 200 µL) at 25 °C for 1 h, rinsed three times again, and treated with ALP-labeled anti-rabbit IgG (1:10,000 dilution, 200 µL) at 25 °C for 1 h. After removing excess ALP-labeled anti-rabbit IgG through the washing step, 9.6 mM of 200 µL AAP in Tris–borate (20 mM, pH 9.8) was incubated with each well at 30 °C for 30 min. Subsequently, an aqueous solution of Ag^+-deposited MoS_2 QDs (0.1 mg mL^{-1} of 25 µL MoS_2 QDs and 10 mM of 25 µL $AgNO_3$) was injected into each well. After waiting for 10 min for the in situ growth of AgNPs. The resultant solution's absorption and fluorescence spectra were measured under the same conditions as those mentioned above. To evaluate the complex matrix's effect on the proposed system, samples of human plasma (100 µL; Sigma-Aldrich, No. P9523) were spiked with different concentrations of the normal rabbit IgG (100 µL, 0–4 ng mL-1). Subsequently, the rabbit IgG-spiked samples were analyzed by the proposed integrated system.

Results and discussion

Fabrication of the Ag^+-deposited MoS_2 QDs The MoS_2 QDs were fabricated through the DMF-induced exfoliation of layered MoS_2 powder and centrifugation-mediated removal of MoS_2 nanosheets. Electron microscopy and spectroscopic techniques revealed that the as-made MoS_2 QDs had a lateral size of 2.0 ± 0.5 nm (Fig. 1a), interplanar spacing of 0.23 nm (Fig. 1b), a topographic height of 0.89 ± 0.06 nm (Fig. S1; see Supplementary Information in the Electronic Supplementary Materials [ESM]), and excitation-dependent emission behavior (Fig. S2, ESM). In addition, the MoS_2 QDs exhibited high colloidal stability under conditions of 0–1 M NaCl (Fig. S3, ESM), pH 3–11 (Fig. S4, ESM), and long-term ultraviolet exposure (Fig. S5, ESM). These findings suggest that the proposed synthetic method endows monolayer MoS_2 QDs with exceptional optical properties. Given that the particle size of the MoS_2 QDs was < 5 nm [51], the proposed synthesis procedure was successful in converting layered MoS_2 to the MoS_2 QDs. To understand the binding effect of Ag^+ on the colloidal stability of the MoS_2 QDs, we measured the morphology and surface charges of the MoS_2 QDs before and after the addition of the Ag^+ ions. According to the TEM images, the lateral sizes of the Ag^+-deposited MoS_2 QDs were 5.9 ± 1.7 nm ($n = 100$; Fig. 1c). This indicates that the Ag^+ ions triggered the assembly of the MoS_2 QDs, leading to an increase in their particle size. To corroborate the aforementioned results, we determined the elemental composition of the Ag^+-free and Ag^+-deposited MoS_2 QDs using TEM with EDS. The EDS spectrum of the Ag^+-deposited MoS_2 QDs exhibited an additional Ag peak compared with the EDS spectrum of the MoS_2 QDs (Fig. 1d and e). We next examined the surface charge characteristics of the MoS_2 QDs in 20 mM Tris–borate buffer (pH 9.8). As the Ag^+ concentration varied from 5 to 20 mM, the zeta potential of the MoS_2 QDs varied significantly from −31 to +6 mV (Fig. 1f). These findings verified that Ag^+ ions were firmly attached to the unbound sulfur sites of MoS_2 QDs due to the coordination of electron-deficient Ag^+ ions and electron-rich sulfur atoms [52]. The deposited Ag^+ ions can serve as nuclei to form AgNPs in the presence of suitable reducing agents [53].

The Ag^+-deposited MoS_2 QDs for triplet-modal sensing of ALP The successful synthesis of the Ag^+-deposited MoS_2 QDs encouraged us to develop a trimodal platform for sensing ALP. Figure 2A illustrates the integration of the Ag^+-deposited MoS_2 QDs with the ALP-mediated hydrolysis of AAP to AA for sensing ALP activity. The proposed sensing procedure proceeds in three steps: (1) ALP promotes the hydrolysis of AAP to AA in an alkaline environment; (2) the resultant AA triggers the reduction of the bound Ag^+ ions to AgNPs on the MoS_2 QD surface; and (3) the resultant AgNPs exhibit intense SPR in the visible region, trigger the fluorescence quenching of the MoS_2 QDs through the fluorescence resonance energy transfer process [54], and shorten the fluorescence lifetime of the MoS_2 QDs. To validate this procedure, the fluorescence and absorption spectra (illustrated in Fig. 2B and C, respectively) of the MoS_2 QDs and the Ag^+-deposited MoS_2 QDs were measured in the presence of ALP (2.5 units L^{-1}) and AAP (9.6 mM). A

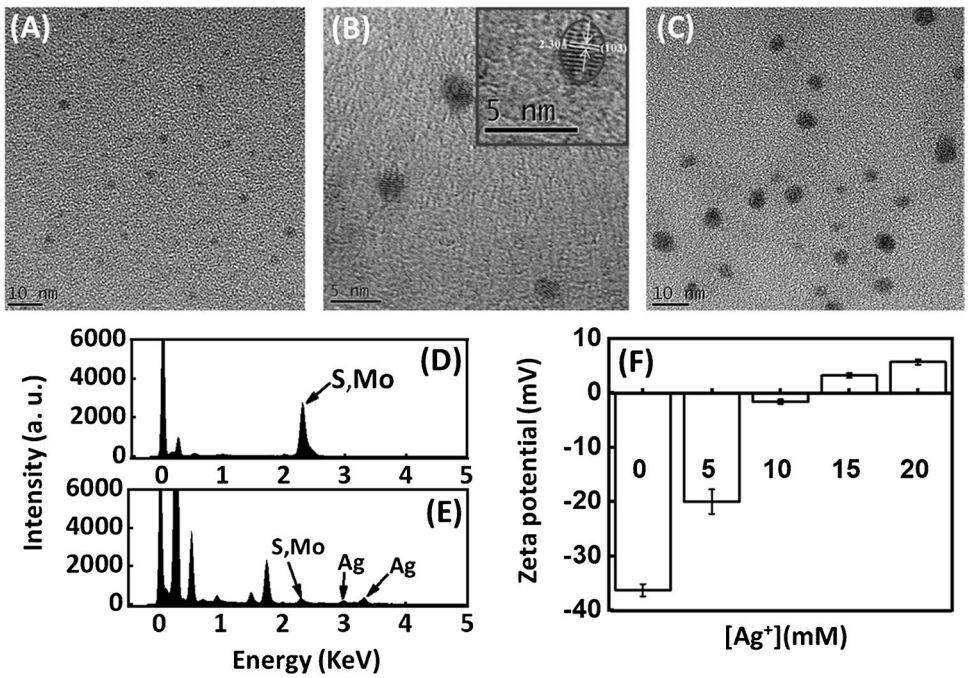

Fig. 1 Comparison of the MoS_2 QDs and Ag^+-deposited MoS_2 QDs. **a**, **b**, **c** TEM images of **a**, **b** the MoS_2 QDs and **c** the Ag^+-deposited MoS_2 QDs. Inset in **b**: high-resolution TEM image of the MoS_2 QDs. **d**, **e** EDS spectra of **d** the MoS_2 QDs and **e** the Ag^+-deposited MoS_2 QDs. **f** Zeta potential of the MoS_2 QDs as a function of the Ag^+ concentration. The concentrations of the MoS_2 QDs were 0.5 mg mL^{-1}. The reactions of the MoS_2 QDs and Ag^+ ions were conducted in 20 mM Tris–borate buffer (pH 9.8)

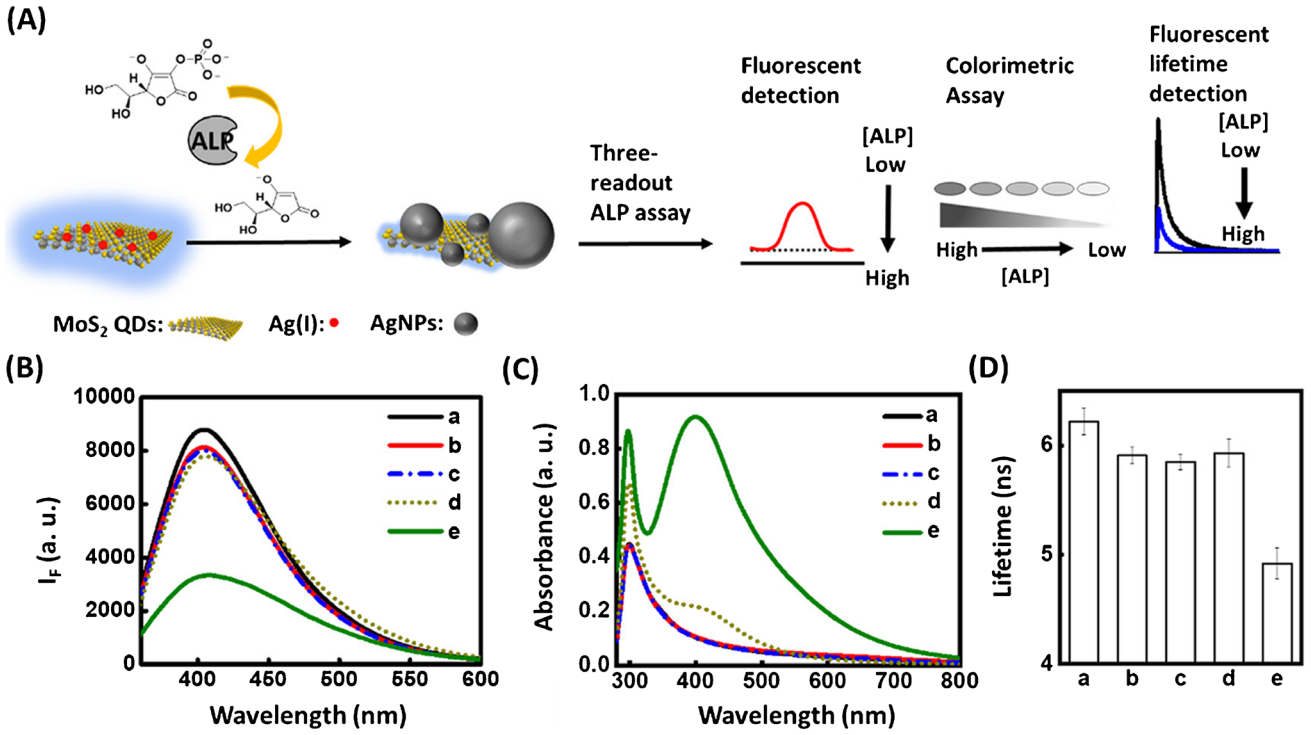

Fig. 2 Triple-modal sensing of ALP. **A** Schematic illustration of the procedure associated with the integration of the Ag^+-deposited MoS_2 QDs and the ALP-mediated hydrolysis of AAP for triplet-modal sensing of ALP. **B** Fluorescence spectra, **C** absorption spectra, and **D** fluorescence lifetime of solution containing (a) the MoS_2, (b) the Ag^+-deposited MoS_2 QDs, (c) the Ag^+-deposited MoS_2 QDs and ALP, (d) the Ag^+-deposited MoS_2 QDs and AAP, and (e) the Ag^+-deposited MoS_2 QDs, AAP, and ALP. The concentrations of the MoS_2 QDs, the Ag^+-deposited MoS_2 QDs, ALP, and AAP were 0.5 mg mL^{-1}, 0.5 mg mL^{-1}, 2.5 units L^{-1}, and 9.6 mM, respectively. All reactions were conducted in 20 mM Tris–borate buffer (pH 9.8). "I_F" represents "fluorescence intensity"

comparison of the fluorescence spectra of the MoS_2 QDs with those of the Ag^+-deposited MoS_2 QDs indicated that the Ag^+ ions slightly suppressed the fluorescence of the MoS_2 QDs in the 20 mM Tris–borate (pH 9.8; curves a and b in Fig. 2B). This slight quenching could result from the Ag^+-promoted aggregation of the MoS_2 QDs [55]. The incubation of the MoS_2 QDs with Ag^+ ions in 20 mM HEPES, phosphate, or carbonate buffer induced efficient fluorescence quenching (Fig. S6, ESM). Curves c and d in Fig. 2B indicate that the incubation of the Ag^+-deposited MoS_2 QDs with either ALP or AAP exerted a negligible effect on their fluorescence intensity. The MoS_2 QDs (curve a in Fig. 2C) exhibited absorption profiles similar to those of the Ag^+-deposited MoS_2 QDs (curve b in Fig. 2C) and of a mixture of ALP and Ag^+-deposited MoS_2 QDs (curve c in Fig. 2C). By contrast, the addition of AAP to the Ag^+-deposited MoS_2 QDs generated a weak SPR peak, signifying that a small portion of AAP was hydrolyzed to AA (curve d in Fig. 2C). However, a small amount of AgNPs is insufficient to quench the fluorescence of the MoS_2 QDs. After ALP catalyzed the hydrolysis of AAP, the resultant AA activated the reduction of Ag^+ ions to AgNPs on the MoS_2 QD surface. Consequently, the AgNPs exhibited a strong SPR peak at 403 nm that efficiently quenched the fluorescence of the MoS_2 QDs (curve e in Fig. 2B and C). The SPR peak at 403 nm indicated that the particle size of the resultant AgNPs was approximately 25 nm with an extinction coefficient of 8×10^9 M^{-1} cm^{-1} [56]. The fluorescence lifetimes of the MoS_2 QDs and Ag^+-deposited MoS_2 QDs measured under the same testing conditions were 6.22 and 5.91 ns, respectively, which is consistent with the results obtained after Ag^+-mediated fluorescence quenching of the MoS_2 QDs (Fig. 2D). Furthermore, the fluorescence lifetime of the Ag^+-deposited MoS_2 QDs remained almost constant upon the addition of ALP or AAP; however, when the products from the reaction of AAP and ALP were added, the fluorescence lifetime of the Ag^+-deposited MoS_2 QDs decreased to 4.91 ns. These results indicate that the Ag^+-deposited MoS_2 QDs are well suited for the colorimetric, fluorescent, and fluorescence-lifetime sensing of ALP. To validate the aforementioned results, the products of the reaction of the Ag^+-deposited MoS_2 QDs, AAP, and ALP were examined using TEM, high-resolution TEM, and dynamic light scattering (DLS; Figs. S7 and S8, ESM). The TEM images and DLS spectra revealed that the inorganic core size (approximately 10–30 nm) and hydrodynamic

diameter (22 ± 5 nm) of the products were much larger than those of the Ag^+-deposited MoS_2 QDs. The resultant AA was capable of reducing the bound Ag^+ ions to AgNPs on the surface of the Ag^+-deposited MoS_2 QDs, which is a cause of the aforementioned phenomenon.

We then explored the mechanism underlying the AgNPs-mediated fluorescence quenching of the MoS_2 QDs using the Stern–Volmer equation. To fabricate different concentrations of the AgNPs (quenchers) on the MoS_2 surface, samples of various ALP concentrations reacted with a fixed concentration of AAP for 30 min, and the Ag^+-deposited MoS_2 QDs were incubated in Tris–borate buffer. The concentration (c) of the resultant AgNPs was estimated according to the Beer–Lambert law, $A = \epsilon bc$ (where A is the absorbance at 403 nm, ϵ is 8×10^9 M^{-1} cm^{-1}, and b is 1.0 cm). As illustrated in Fig. S9 (ESM), a positively sloped Stern–Volmer plot was constructed by plotting the I_{F0}/I_F ratio against the AgNP concentration; I_{F0} and I_F correspond to the fluorescence intensity of the Ag^+-deposited MoS_2 QD at 407 nm before and after the ALP-mediated formation of AgNPs, respectively, at a fixed concentration of AAP. This nonlinear plot with a large positive deviation signifies that the AgNP-mediated fluorescence quenching of the MoS_2 QDs involved both dynamic and static quenching processes. Moreover, the ratio of the fluorescence lifetime of the Ag^+-deposited MoS_2 QDs (τ_0) to that of the AgNPs–MoS_2 QD composites (τ_1) increased linearly with ALP concentration (Fig. S10, ESM). This linear plot verified the occurrence of dynamic quenching between the AgNPs and MoS_2 QDs and yielded a dynamic quenching constant (K_D) of 1.969×10^9 M^{-1}. However, an increase in the concentration of the quenchers (i.e., AgNPs) led to a larger change in the I_{F0}/I_F value than in the τ_0/τ_1 value. If the AgNP-mediated quenching process of the MoS_2 QDs was identical to the dynamic quenching process, then $I_{F0}/I_F = \tau_0/\tau_1$. Thus, our observations imply that the quenching of the MoS_2 QDs by the AgNPs mainly resulted from static quenching [57]. These results are consistent with those of previous studies, which have examined the mixed dynamic and static quenching of 4-aryloxymethyl coumarin dyes [58], transmembrane proteins [59], and tryptamine [60] by AgNPs.

Sensitivity, selectivity, and application To test the sensitivity of our proposed platform in different detection modes, we conducted a reaction of 0–4 units L^{-1} ALP and 9.6 mM AAP at 37 °C in 20 mM Tris–borate (pH 9.8) for 30 min. The resultant products were incubated with the Ag^+-deposited MoS_2 QDs at ambient temperature for 10 min. Consequently, a progressive increase in the ALP activity led to a reduction in the fluorescence intensity of the MoS_2 QDs (Fig. 3A), an increase in the intensity of the AgNP-related SPR peaks (Fig. 3B), and a reduction in the fluorescence lifetime of the MoS_2 QDs (Fig. 3C). The $(I_{F1} - I_{F2})/I_{F1}$ value obtained from the Ag^+-deposited MoS_2 QDs increased linearly ($R^2 = 0.9944$) as the ALP activity increased from 0.05 to 2.5 units L^{-1} (Fig. 3D); I_{F1} and I_{F2} correspond to the fluorescence intensity of the Ag^+-deposited MoS_2 QDs at 407 nm before and after adding the AA products, respectively. In addition, plotting the intensity of the SPR band at 403 nm and the fitted fluorescence lifetime against the ALP activity generated linear calibration curves for quantifying 0.1–4 units L^{-1} of ALP ($R^2 = 0.9980$; Fig. 3E) and 1–4 units L^{-1} of ALP ($R^2 = 0.9687$; Fig. 3F), respectively. The triple-modal platform allows the fluorescent, colorimetric, and fluorescence-lifetime sensing of the ALP activity to achieve limits of detection (LODs; signal-to-noise ratio = 3.0) of 0.01, 0.085, and 0.3 units L^{-1}, respectively. The LODs of ALP measured from the triple-readout probe in this study are comparable with those detected by single- and dual-readout QD-based probes in previous studies, including those based on boron nitride (0.8 units L^{-1}) [61], N-doped carbon (1.1 units L^{-1}) [62], MoS_2 (0.1 units L^{-1}) [63], sulfanilic acid–capped graphene (0.045 units L^{-1}) [64], CuInS ZnS (0.01 units L^{-1}) [65], and nitrogen- and sulfur-doped graphene (0.009 and 0.005 units L^{-1}) [40] QDs. Moreover, a progressive increase in ALP activity caused the probe to change color from light brown to dark brown (inset in Fig. 3C). The probe allows for naked-eye detection of concentrations of ALP activity (0.5 units L^{-1}) that are lower than those reported in studies employing other methods, including those using horseradish peroxidase catalytic (for colorimetry; 20 units L^{-1}) [66], azide alkyne functionalized gold nanoparticles (5 units L^{-1}) [67], silver-deposited gold nanorods (40 units L^{-1}) [68], and polydopamine nanoparticle–adsorbed MnO_2 nanosheets (1 unit L^{-1}) [69]. Specifically, the probe can differentiate between 0.0, 0.5, 1.0, 1.5, and 2.0 units L^{-1} of ALP, indicating that its resolution is up to 0.5 units L^{-1}. The selectivity of the probe was evaluated by substituting ALP with other common enzymes and proteins, including thrombin, glucose oxidase, horseradish peroxidase, human serum albumin, lysozyme, and bovine serum albumin. As indicated in Fig. 3G, H, and I, only ALP promoted a remarkable increase in $(I_{F1} - I_{F2})/I_{F1}$ value, absorbance at 403 nm, and fluorescence lifetime. This result indicates that the probe is highly responsive to the ALP activity in the fluorescent, colorimetric, and fluorescence-lifetime detection modes. However, the probe may have the disadvantage of poor selectivity for ALP in the presence of reductive compounds such as cysteine, dopamine, and AA. Due to the low molecular weights of reductive compounds, interference from such compounds might be suppressed by an ultrafiltration membrane process for pretreating the sample. To verify the effect of the MoS_2 QDs in the colorimetric mode, we used Ag^+ ions in place of the Ag^+-deposited MoS_2 QDs. The SPR peak of the resultant AgNPs progressively increased with ALP concentration (Fig. S11, ESM).

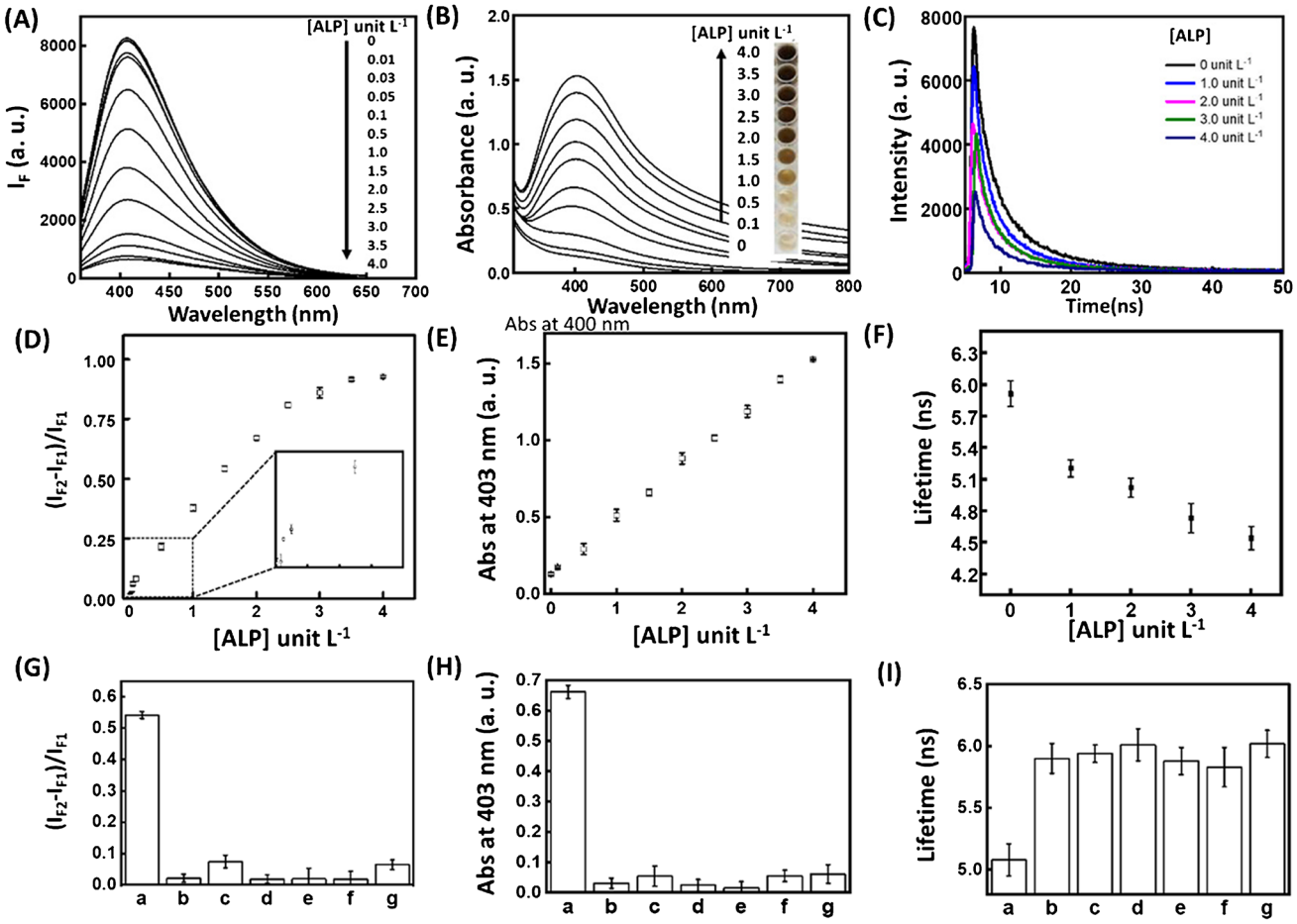

Fig. 3 Sensitivity and selectivity of the Ag^+-deposited MoS_2 QDs. **A**, **B**, **C** The collected **A** fluorescence spectra, **B** absorption spectra, and **C** fluorescence lifetime decay of the Ag^+-deposited MoS_2 QDs as a function of the ALP concentration at a fixed concentration of AAP. **D**, **E**, **F** Plots of **D** the $(I_{F1}-I_{F2})/I_{F1}$ value, **E** the SPR band at 403 nm, and **F** the fluorescence lifetime versus the ALP activity. **G**, **H**, **I** The values of **G** $(I_{F1}-I_{F2})/I_{F1}$, **H** absorbance at 403 nm, and **I** fluorescence lifetime obtained from incubating the present probe with possibly interfering proteins in 20 mM Tris–borate buffer (pH 9.8). Protein: (a) 1.5 unit L^{-1} ALP, (b) 100 nM thrombin, (c) 100 nM glucose oxidase, (d) 100 nM horseradish peroxidase, (e) 100 nM human serum albumin, (f) 100 nM bovine serum albumin, and (g) 100 nM lysozyme. **D**–**I** The error bars represent the standard deviation of three independent measurements. "I_F" and "Abs" indicate "fluorescence intensity" and "absorbance", respectively. The concentrations of the Ag^+-deposited MoS_2 QDs and AAP were 0.5 mg mL^{-1} and 9.6 mM, respectively. All reactions were conducted in 20 mM Tris–borate buffer (pH 9.8)

However, in the absence of the MoS_2 QDs, the LOD and linear range for ALP were determined to be 0.17 units L^{-1} and 0.5–4 units L^{-1}, respectively. This indicates that the use of MoS_2 QDs not only allows for use of the fluorescent and fluorescence-lifetime detection modes but also facilitates the growth of the AgNPs.

Considering that the proposed platform provided the highest sensitivity to ALP in the fluorescent detection mode, we extended its applicability to an ALP-related fluorescent immunoassay. Rabbit IgG was selected to test the sensitivity of the integrated system using a procedure consisting of three main steps. In the first step, the rabbit IgG was captured by a sandwich immunoreaction between anti-rabbit IgG as a capture antibody and ALP-conjugated anti-rabbit IgG as a detection antibody. Subsequently, the conjugated ALP catalyzed the hydrolysis of AAP to AA. Finally, the reaction between the resultant AA molecules and Ag^+-deposited MoS_2 QDs generated fluorometric and colorimetric dual-readout signals. Figure 4a illustrates the aforementioned sensing procedure of the integrated system. As the concentration of rabbit IgG varied from 0 to 1000 pg mL^{-1}, we observed a progressive reduction in the fluorescence of the Ag^+-deposited MoS_2 QDs and a color transition from transparent to light brown to dark brown (Fig. 4b). We plotted the $(I_{F3}-I_{F4})/I_{F3}$ values against the logarithm of IgG concentration over the range 25–1000 pg mL^{-1} to generate a linear calibration curve ($R^2=0.9834$), as presented in Fig. 4c; I_{F3} and I_{F4} were equal to the fluorescence intensity of the Ag^+-deposited MoS_2 QDs at 407 nm in the absence and presence of rabbit IgG, respectively, in the integrated

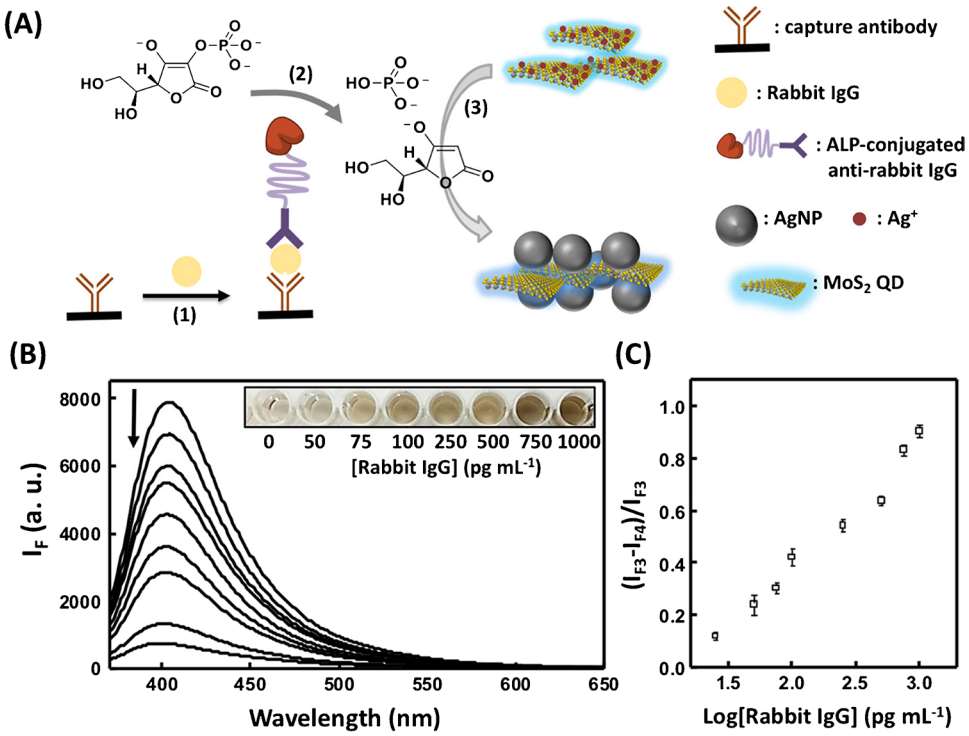

Fig. 4 Sensing of rabbit IgG by dual-readout immunoassay. **a** Schematic illustration of the procedure associated with the integration of (1) antibody-antigen recognition, (2) ALP-catalyzed hydrolysis of AAP to AA, and (3) AA-induced reduction of Ag^+ to AgNPs on the MoS_2 QDs. **b** Fluorescence spectra and colorimetric images obtained from the detection of 0–1000 pg mL^{-1} rabbit IgG by the proposed dual-readout immunoassay. The arrow indicates the variation in the fluorescence signal with an increased concentration of rabbit IgG (0, 25, 50, 75, 100, 250, 500, 750, and 1000 pg mL^{-1}). **c** A plot of the $(I_{F3} - I_{F4})/I_{F3}$ value versus the logarithm of the rabbit IgG concentration. The error bars represent the standard deviation of three independent measurements. "I_F" indicates "fluorescence intensity"

system. Commercially available kits from Abcam (Rabbit IgG ELISA Kit, Abcam, Cambridge, UK, catalog number: ab187400) and Thermo Fisher Scientific (Easy-Titer Rabbit IgG Assay Kit, Thermo Fisher Scientific, Waltham, MA, USA, catalog number: 23305) indicated that the quantification ranges of rabbit IgG were 0.31–20 and 8–500 ng mL^{-1}, respectively. The LOD and visual LOD of the rabbit IgG, detected by the fluorescence immunoassay and the naked eye, were 8 and 75 pg mL^{-1}, respectively. The sensitivity of our proposed platform for rabbit IgG is comparable to those of immunoassays involving ultrasensitive electrochemical detection, hydrogen evolution reactions, or electron spin resonance (Table S1, ESM). Moreover, the sensitivity of the Ag^+-deposited MoS_2 QDs as signal reporters in the sandwich immunoassay was superior to that of the previously reported organic substrates and nanomaterials (Table S1, ESM). The effect of the sample matrix on the performance of the proposed fluorescence immunoassay was evaluated by spiking human plasma with a series of rabbit IgG standards with known concentrations. As expected, the fluorescence of the Ag^+-deposited MoS_2 QDs was incrementally quenched with increasing spiked concentration of the rabbit IgG in the human plasma (Fig. S12, ESM). A linear calibration curve for quantifying 25–1000 pg mL^{-1} rabbit IgG was constructed by plotting the $(I_{F3} - I_{F4})/I_{F3}$ values against the spiked concentration of rabbit IgG. The difference in the slope of the calibration curve between the standard and spiked samples was estimated to be < 10%, indicating that the matrix of the plasma sample does not significantly affect the sensitivity and selectivity of the integrated system. The proposed system provides high visual sensitivity for the detection of 75–1000 pg mL^{-1} rabbit IgG in human plasma. Thus, the probe paired with the ALP-related immunoassay may provide a new method for the accurate, sensitive, and selective analysis of various biomolecules in clinical samples through the use of specific antibodies.

Conclusions

We developed a triple-readout probe for the fluorescent and colorimetric sensing of ALP activity based on the ALP-mediated dephosphorylation of AAP to AA and the AA-triggered in situ reduction of Ag^+ ions to AgNPs on the surface of MoS_2 QDs. The Ag^+-deposited MoS_2 QDs were fabricated by coordinating Ag^+ ions with sulfur atoms of the MoS_2 QDs. The reaction of the AA and Ag^+-deposited MoS_2 QDs generated the SPR peaks of the AgNPs, which (1) promoted the fluorescence quenching of the MoS_2 QDs through a mix of static and dynamic quenching and (2) induced the reduction in the fluorescence lifetime of the MoS_2 QDs through the dynamic quenching process. Moreover, the fluorescent detection mode of the proposed triple-readout probe was determined to be well integrated with the ALP-related sandwich immunoassay. The proposed platform allows for the fluorescent detection of rabbit IgG in concentrations as low as 25 pg mL^{-1}, which indicates a sensitivity

comparable with that of immunoassays involving ultrasensitive electrochemical detection, hydrogen evolution reactions, or electron spin resonance. Additionally, the visual LOD of the proposed system for rabbit IgG was 75 pg mL^{-1}, which is lower than the visual LODs of metal nanoparticle–based ELISA assays (Table S2, ESM) and commercially available kits. Our proposed probe can be directly incorporated with commercially available ALP-conjugated antibodies without further conjugation of signal reporters. When integrated with ALP-related sandwich immunoassays, this probe will serve as a sensitive platform for the detection of various biological analytes in clinical diagnosis.

Supplementary Information The online version contains supplementary material available at https://doi.org/10.1007/s00216-021-03826-2.

Acknowledgements We would like to thank the Ministry of Science and Technology of Taiwan (MOST107-2113-M-110-013-MY3; MOST 110-2113-M-017-002-MY3) and NSYSU-KMU Joint Research Project (NSYSUKMU 109-P002) for the financial support of this study.

Author contribution Manivannan Madhu: Methodology, Investigation, Formal analysis, Visualization, Writing – original draft. Chien-Min Chao: Investigation, Formal analysis. Chen-Yi Ke: Investigation, Formal analysis, Visualization. Ming-Mu Hsieh: Conceptualization, Methodology, Resources, Writing – original draft, Writing – review & editing, Supervision, Funding acquisition. Wei-Lung Tseng: Conceptualization, Methodology, Resources, Writing – original draft, Writing – review & editing, Supervision, Funding acquisition.

Declarations

Conflicts of interests The authors declare that they have no known competing financial interests or personal relationships that could have appeared to influence the work reported in this paper.

References

1. Zhang L, Buchet R, Azzar G. Phosphate binding in the active site of alkaline phosphatase and the interactions of 2-nitrosoacetophenone with alkaline phosphatase-induced small structural changes. Biophys J. 2004;86(6):3873–81.
2. Nikolic-Hughes I, O'brien PJ, Herschlag D. Alkaline phosphatase catalysis is ultrasensitive to charge sequestered between the active site zinc ions. J Am Chem Soc. 2005;127(26):9314–5.
3. Hausamen TU, Helger R, Rick W, Gross W. Optimal conditions for the determination of serum alkaline phosphatase by a new kinetic method. Clin Chim Acta. 1967;15(2):241–5.
4. Abdallah EAA, Said RN, Mosallam DS, Moawad EMI, Kamal NM, Fathallah MGE. Serial serum alkaline phosphatase as an early biomarker for osteopenia of prematurity. Medicine (Baltimore). 2016;95(37):e4837
5. Li D, Lv H, Hao X, Hu B, Song Y. Prognostic value of serum alkaline phosphatase in the survival of prostate cancer: evidence from a meta-analysis. Cancer Manag Res. 2018;10:3125.
6. Chen WZ, Shen JF, Zhou Y, Chen XY, Liu JM, Liu ZL. Clinical characteristics and risk factors for developing bone metastases in patients with breast cancer. Sci Rep. 2017;7(1):1–7.
7. Chen SC, Tsai SP, Jhao JY, Jiang WK, Tsao CK, Chang LY. Liver fat, hepatic enzymes, alkaline phosphatase and the risk of incident type 2 diabetes: a prospective study of 132,377 adults. Sci Rep. 2017;7(1):1–9.
8. Giannini EG, Testa R, Savarino V. Liver enzyme alteration: a guide for clinicians. Can Med Assoc J. 2005;172(3):367–79.
9. Lucarelli F, Marrazza G, Mascini M. Dendritic-like streptavidin/alkaline phosphatase nanoarchitectures for amplified electrochemical sensing of DNA sequences. Langmuir. 2006;22(9):4305–9.
10. Florentinus-Mefailoski A, Marshall JG. Linear quantification of a streptavidin–alkaline phosphatase probe for enzyme-linked immuno mass spectrometric assay. Anal Biochem. 2016;503:50–5.
11. Selvolini G, Lettieri M, Tassoni L, Gastaldello S, Grillo M, Maran C, et al. Electrochemical enzyme-linked oligonucleotide array for aflatoxin B1 detection. Talanta. 2019;203:49–57.
12. Sun Z, Wang X, Chen Q, Yun Y, Tang Z, Liu X. Nanobody-alkaline phosphatase fusion protein-based enzyme-linked immunosorbent assay for one-step detection of ochratoxin A in rice. Sensors. 2018;18(11):4044.
13. Gao Z, Hou L, Xu M, Tang D. Enhanced colorimetric immunoassay accompanying with enzyme cascade amplification strategy for ultrasensitive detection of low-abundance protein. Sci Rep. 2014;4(1):1–8.
14. Liu Y, Schanze KS. Conjugated polyelectrolyte-based real-time fluorescence assay for alkaline phosphatase with pyrophosphate as substrate. Anal Chem. 2008;80(22):8605–12.
15. Zhang L, Zhao J, Duan M, Zhang H, Jiang J, Yu R. Inhibition of dsDNA-templated copper nanoparticles by pyrophosphate as a label-free fluorescent strategy for alkaline phosphatase assay. Anal Chem. 2013;85(8):3797–801.
16. Bhimji A, Zaragoza AA, Live LS, Kelley SO. Electrochemical enzyme-linked immunosorbent assay featuring proximal reagent generation: detection of human immunodeficiency virus antibodies in clinical samples. Anal Chem. 2013;85(14):6813–9.
17. Liu H, Wei L, Hua J, Chen D, Meng H, Li Z, et al. Enzyme activity-modulated etching of gold nanobipyramids@ MnO 2 nanoparticles for ALP assay using surface-enhanced Raman spectroscopy. Nanoscale. 2020;12(18):10390–8.
18. Han Y, Chen J, Li Z, Chen H, Qiu H. Recent progress and prospects of alkaline phosphatase biosensor based on fluorescence strategy. Biosens Bioelectron. 2020;148:111811.
19. Kong RM, Fu T, Sun NN, Qu FL, Zhang SF, Zhang XB. Pyrophosphate-regulated Zn2+-dependent DNAzyme activity: An amplified fluorescence sensing strategy for alkaline phosphatase. Biosens Bioelectron. 2013;50:351–5.
20. Chen C, Yuan Q, Ni P, Jiang Y, Zhao Z, Lu Y. Fluorescence assay for alkaline phosphatase based on ATP hydrolysis-triggered dissociation of cerium coordination polymer nanoparticles. Analyst. 2018;143(16):3821–8.
21. Cao XY, Kong FZ, Zhang Q, Liu WW, Liu XP, Li GQ, et al. iPhone-imaged and cell-powered electrophoresis titration chip for the alkaline phosphatase assay in serum by the moving reaction boundary. Lab Chip. 2018;18(12):1758–66.
22. Liu H, Li M, Xia Y, Ren X. A turn-on fluorescent sensor for selective and sensitive detection of alkaline phosphatase activity with gold nanoclusters based on inner filter effect. ACS Appl Mater Interfaces. 2017;9(1):120–6.
23. Chen P, Yan S, Sawyer E, Ying B, Wei X, Wu Z, et al. Rapid and simple detection of ascorbic acid and alkaline phosphatase via controlled generation of silver nanoparticles and selective recognition. Analyst. 2019;144(4):1147–52.
24. Wang F, Li Y, Li W, Zhang Q, Chen J, Zhou H, et al. A facile method for detection of alkaline phosphatase activity based on the turn-on fluorescence of resorufin. Anal Methods. 2014;6(15):6105–9.

25. Zhao D, Li J, Peng C, Zhu S, Sun J, Yang X. Fluorescence immunoassay based on the alkaline phosphatase triggered in situ fluorogenic reaction of o-phenylenediamine and ascorbic acid. Anal Chem. 2019;91(4):2978–84.
26. Sun J, Hu T, Chen C, Zhao D, Yang F, Yang X. Fluorescence immunoassay system via enzyme-enabled in situ synthesis of fluorescent silicon nanoparticles. Anal Chem. 2016;88(19):9789–95.
27. Hu Q, Zhou B, Li F, Kong J, Zhang X. Turn-on colorimetric platform for dual activity detection of acid and alkaline phosphatase in human whole blood. Chem Asian J. 2016;11(21):3040–5.
28. Hu L, Zhang Q, Gan X, Lin S, Han S, Zhang Z. Fluorometric turn-on determination of the activity of alkaline phosphatase by using WS 2 quantum dots and enzymatic cleavage of ascorbic acid 2-phosphate. Microchim Acta. 2018;185(8):1–6.
29. Ni P, Chen C, Jiang Y, Zhang C, Wang B, Cao B, et al. Gold nanoclusters-based dual-channel assay for colorimetric and turn-on fluorescent sensing of alkaline phosphatase. Sens Actuators B Chem. 2019;301:127080.
30. Liang MY, Zhao B, Xiong Y, Chen WX, Huo JZ, Zhang F, et al. A "turn-on" sensor based on MnO 2 coated UCNPs for detection of alkaline phosphatase and ascorbic acid. Dalton Trans. 2019;48(43):16199–210.
31. Pham XH, Hahm E, Kim TH, Kim HM, Lee SH, Lee YS, et al. Enzyme-catalyzed Ag growth on Au nanoparticle-assembled structure for highly sensitive colorimetric immunoassay. Sci Rep. 2018;8(1):1–7.
32. He Y, Jiao B. Determination of the activity of alkaline phosphatase based on the use of ssDNA-templated fluorescent silver nanoclusters and on enzyme-triggered silver reduction. Microchim Acta. 2017;184(10):4167–73.
33. Wang H, Yang L, Chu S, Liu B, Zhang Q, Zou L, et al. Semiquantitative visual detection of lead ions with a smartphone via a colorimetric paper-based analytical device. Anal Chem. 2019;91(14):9292–9.
34. Wang H, Da L, Yang L, Chu S, Yang F, Yu S, et al. Colorimetric fluorescent paper strip with smartphone platform for quantitative detection of cadmium ions in real samples. J Hazard Mater. 2020;392:122506.
35. Chu S, Wang H, Ling X, Yu S, Yang L, Jiang C. A portable smartphone platform using a ratiometric fluorescent paper strip for visual quantitative sensing. ACS Appl Mater Interfaces. 2020;12(11):12962–71.
36. Chu S, Wang H, Du Y, Yang F, Yang L, Jiang C. Portable smartphone platform integrated with a nanoprobe-based fluorescent paper strip: visual monitoring of glutathione in human serum for health prognosis. ACS Sustain Chem Eng. 2020;8(22):8175–83.
37. Liu SG, Han L, Li N, Xiao N, Ju YJ, Li NB, et al. A fluorescence and colorimetric dual-mode assay of alkaline phosphatase activity via destroying oxidase-like CoOOH nanoflakes. J Mater Chem B. 2018;6(18):2843–50.
38. Zhao J, Wang S, Lu S, Bao X, Sun J, Yang X. An enzyme cascade-triggered fluorogenic and chromogenic reaction applied in enzyme activity assay and immunoassay. Anal Chem. 2018;90(12):7754–60.
39. Zhao J, Wang S, Lu S, Liu G, Sun J, Yang X. Fluorometric and colorimetric dual-readout immunoassay based on an alkaline phosphatase-triggered reaction. Anal Chem. 2019;91(12):7828–34.
40. Chen C, Zhang G, Ni P, Jiang Y, Lu Y, Lu Z. Fluorometric and colorimetric dual-readout alkaline phosphatase activity assay based on enzymatically induced formation of colored Au@Ag nanoparticles and an inner filter effect. Microchim Acta. 2019;186(6):348.
41. Zhang J, He L, Zhang X, Wang J, Yang L, Liu B, et al. Colorimetric and SERS dual-readout for assaying alkaline phosphatase activity by ascorbic acid induced aggregation of Ag coated Au nanoparticles. Sens Actuators B Chem. 2017;253:839–45.
42. Gopalakrishnan D, Damien D, Shaijumon MM. MoS2 quantum dot-interspersed exfoliated MoS2 nanosheets. ACS Nano. 2014;8(5):5297–303.
43. Xu G, Yang L, Wei X, Ding J, Zhong J, Chu PK. MoS2-Quantum-Dot-Interspersed Li4Ti5O12 Nanosheets with Enhanced Performance for Li-and Na-Ion Batteries. Adv Funct Mater. 2016;26(19):3349–58.
44. Gu W, Yan Y, Zhang C, Ding C, Xian Y. One-step synthesis of water-soluble MoS2 quantum dots via a hydrothermal method as a fluorescent probe for hyaluronidase detection. ACS Appl Mater Interfaces. 2016;8(18):11272–9.
45. Yue N, Weicheng J, Rongguo W, Guomin D, Yifan H. Hybrid nanostructures combining graphene–MoS 2 quantum dots for gas sensing. J Mater Chem A. 2016;4(21):8198–203.
46. Chen SC, Lin CY, Cheng TL, Tseng WL. 6-mercaptopurine-induced fluorescence quenching of monolayer MoS2 nanodots: applications to glutathione sensing, cellular imaging, and glutathione-stimulated drug delivery. Adv Funct Mater. 2017;27(41):1702452.
47. Wang Z, Sim A, Urban JJ, Mi B. Removal and recovery of heavy metal ions by two-dimensional MoS2 nanosheets: performance and mechanisms. Environ Sci Technol. 2018;52(17):9741–8.
48. Wu MJ, Tseng WL. Rapid, facile, reagentless, and room-temperature conjugation of monolayer MoS 2 nanosheets with dual-fluorophore-labeled flares as nanoprobes for ratiometric sensing of TK1 mRNA in living cells. J Mater Chem B. 2020;8(8):1692–8.
49. Kumar ASK, Tseng W-B, Wu MJ, Huang YY, Tseng WL. L-cystine-linked BODIPY-adsorbed monolayer MoS2 quantum dots for ratiometric fluorescent sensing of biothiols based on the inner filter effect. Anal Chim Acta. 2020;1113:43–51.
50. Lin JH, Yang YC, Shih YC, Hung SY, Lu CY, Tseng WL. Photoinduced electron transfer between Fe (III) and adenosine triphosphate-BODIPY conjugates: application to alkaline-phosphatase-linked immunoassay. Biosens Bioelectron. 2016;77:242–8.
51. Li B, Jiang L, Li X, Ran P, Zuo P, Wang A, et al. Preparation of monolayer MoS 2 quantum dots using temporally shaped femtosecond laser ablation of bulk MoS 2 targets in water. Sci Rep. 2017;7(1):1–12.
52. Cao F, Ju E, Zhang Y, Wang Z, Liu C, Li W, et al. An efficient and benign antimicrobial depot based on silver-infused MoS2. ACS Nano. 2017;11(5):4651–9.
53. Lei Y, Li D, Zhang TC, Huang X, Liu L, Lu Y. One-step selective formation of silver nanoparticles on atomic layered MoS 2 by laser-induced defect engineering and photoreduction. J Mater Chem C. 2017;5(34):8883–92.
54. Zhou J, Chen J, Ge Y, Shao Y. Two-dimensional nanomaterials for Förster resonance energy transfer–based sensing applications. Nanophotonics. 2020;9(7):1855–75.
55. Guo X, Huang J, Zeng Q, Wei Y, Liu X, Wang L. Boronic acid-functionalized molybdenum disulfide quantum dots for the ultrasensitive analysis of dopamine based on synergistic quenching effects from IFE and aggregation. J Mater Chem B. 2019;7(17):2799–807.
56. Paramelle D, Sadovoy A, Gorelik S, Free P, Hobley J, Fernig DG. A rapid method to estimate the concentration of citrate capped silver nanoparticles from UV-visible light spectra. Analyst. 2014;139(19):4855–61.
57. Zhong Y, Yi T. MoS 2 quantum dots as a unique fluorescent "turn-off–on" probe for the simple and rapid determination of adenosine triphosphate. J Mater Chem B. 2019;7(15):2549–56.
58. Raghavendra U, Thipperudrappa J, Basanagouda M, Melavanki R. Influence of silver nanoparticles on spectroscopic properties of biologically active iodinated 4-aryloxymethyl coumarin dyes. J Lumin. 2016;172:139–46.
59. Gambucci M, Tarpani L, Zampini G, Massaro G, Nocchetti M, Sassi P, et al. Fluorimetric studies of a transmembrane protein and

its interactions with differently functionalized silver nanoparticles. J Phys Chem B. 2018;122(27):6872–9.
60. Deng H, Yu H. Silver nanoparticle surface enabled self-assembly of organic dye molecules. Materials. 2019;12(16):2592.
61. Han Y, Niu Y, Liu M, Niu F, Xu Y. A rational strategy to develop a boron nitride quantum dot-based molecular logic gate and fluorescent assay of alkaline phosphatase activity. J Mater Chem B. 2019;7(6):897–902.
62. Niu F, Ying YL, Hua X, Niu Y, Xu Y, Long YT. Electrochemically generated green-fluorescent N-doped carbon quantum dots for facile monitoring alkaline phosphatase activity based on the Fe3+-mediating ON-OFF-ON-OFF fluorescence principle. Carbon. 2018;127:340–8.
63. Zhong Y, Xue F, Wei P, Li R, Cao C, Yi T. Water-soluble MoS 2 quantum dots for facile and sensitive fluorescence sensing of alkaline phosphatase activity in serum and live cells based on the inner filter effect. Nanoscale. 2018;10(45):21298–306.
64. Na W, Li N, Xingguang S. Enzymatic growth of single-layer MnO2 nanosheets in situ: application to detect alkaline phosphatase and ascorbic acid in the presence of sulfanilic acid functionalized graphene quantum dots. Sens Actuators B Chem. 2018;274:172–9.
65. Zhang F, He X, Ma P, Sun Y, Wang X, Song D. Rapid aqueous synthesis of CuInS/ZnS quantum dots as sensor probe for alkaline phosphatase detection and targeted imaging in cancer cells. Talanta. 2018;189:411–7.
66. Shi D, Sun Y, Lin L, Shi C, Wang G, Zhang X. Naked-eye sensitive detection of alkaline phosphatase (ALP) and pyrophosphate (PPi) based on a horseradish peroxidase catalytic colorimetric system with Cu (ii). Analyst. 2016;141(19):5549–54.
67. Xianyu Y, Wang Z, Jiang X. A plasmonic nanosensor for immunoassay via enzyme-triggered click chemistry. ACS Nano. 2014;8(12):12741–7.
68. Gao Z, Deng K, Wang X-D, Miró M, Tang D. High-resolution colorimetric assay for rapid visual readout of phosphatase activity based on gold/silver core/shell nanorod. ACS Appl Mater Interfaces. 2014;6(20):18243–50.
69. Xiao T, Sun J, Zhao J, Wang S, Liu G, Yang X. FRET effect between fluorescent polydopamine nanoparticles and MnO2 nanosheets and its application for sensitive sensing of alkaline phosphatase. ACS Appl Mater Interfaces. 2018;10(7):6560–9.